© 2019. Published by The Company of Biologists Ltd | Journal of Cell Science (2019) 132, jcs223008. doi:10.1242/jcs.223008

RESEARCH ARTICLE

Atrophy, oxidative switching and ultrastructural defects in skeletal muscle of the ataxia telangiectasia mouse model

Valentina Tassinari[1,2,*], Vincenzo De Gennaro[1,3,*], Gina La Sala[4], Daniela Marazziti[4], Giulia Bolasco[5], Salvatore Aguanno[1], Luciana De Angelis[1], Fabio Naro[1] and Manuela Pellegrini[1,4,‡]

ABSTRACT

Ataxia telangiectasia is a rare, multi system disease caused by ATM kinase deficiency. *Atm*-knockout mice recapitulate premature aging, immunodeficiency, cancer predisposition, growth retardation and motor defects, but not cerebellar neurodegeneration and ataxia. We explored whether Atm loss is responsible for skeletal muscle defects by investigating myofiber morphology, oxidative/glycolytic activity, myocyte ultrastructural architecture and neuromuscular junctions. *Atm*-knockout mice showed reduced muscle and fiber size. Atrophy, protein synthesis impairment and a switch from glycolytic to oxidative fibers were detected, along with an increase of in expression of slow and fast myosin types (*Myh7*, and *Myh2* and *Myh4*, respectively) in tibialis anterior and solei muscles isolated from *Atm*-knockout mice. Transmission electron microscopy of tibialis anterior revealed misalignments of Z-lines and sarcomeres and mitochondria abnormalities that were associated with an increase in reactive oxygen species. Moreover, neuromuscular junctions appeared larger and more complex than those in *Atm* wild-type mice, but with preserved presynaptic terminals. In conclusion, we report for the first time that *Atm-knockout* mice have clear morphological skeletal muscle defects that will be relevant for the investigation of the oxidative stress response, motor alteration and the interplay with peripheral nervous system in ataxia telangiectasia.

KEY WORDS: Atm, Skeletal muscle, ROS, Atrophy, Slow myosin, Myopathy

INTRODUCTION

Ataxia telangiectasia (A-T) is a rare genetic disorder caused by mutations in *ATM* gene that cause ATM kinase instability and loss of function (Uziel et al., 1996). In humans, A-T is characterized by progressive ataxia, neurodegeneration, premature aging, immunodeficiency and cancer predisposition that ultimately leads to death within the fourth decade of life (Gatti et al., 1988; Micol et al., 2011). Pathoanatomical studies show degeneration of cerebellar Purkinje cells as the prominent hallmark of the disease, although some studies suggest concomitant alteration of extracerebellar structures, such as the brainstem and basal ganglia (Hoche et al., 2012; Kieslich et al., 2010; Lavin et al., 2007). As a consequence of cerebellar defects, patients may show several secondary abnormalities in eye movement, breathing and fine motor skill control (Hoche et al., 2012; Kieslich et al., 2010). Many patients also exhibit somatic growth retardation and growth factor deficiency (Hoche et al., 2012; Schubert et al., 2005; Voss et al., 2014). In particular, central cerebral white matter affection, spinal atrophy and extrapyramidal symptoms are more often observed in patients with pronounced deficiency of the growth hormone/insulin-like growth factor 1 (GH/IGF-1) axis and with markedly reduced body weight and high ataxia scores (Hoche et al., 2012; Schubert et al., 2005; Voss et al., 2014). *Atm*-null mice recapitulate most of the characteristics of A-T patients, including extreme radiosensitivity, immune system deficiency, germ cell defects and cancer predisposition (Barlow et al., 1996; Elson et al., 1996; Xu et al., 1996). Like A-T patients, mice homozygous for *Atm* disruption are smaller in size than *Atm* wild-type and heterozygous mice (Barlow et al., 1996; Di Siena et al., 2018). The body size difference is already present at birth and becomes more evident throughout the growing period, indicating a direct effect of Atm lack on cellular growth. Mice homozygous for the disruption of *Atm* gene also show defects in exercise performance such as rota-rod, open-field and hind-paw footprint motor function abnormalities; however, they do not exhibit histological brain abnormalities, including cerebellar architecture defects and Purkinje cell degeneration (Barlow et al., 1996; Browne et al., 2004; Reliene et al., 2008).

ATM protein is a key player in cell cycle checkpoint control and DNA repair after DNA double-strand breaks (DSBs) caused by endogenous sources, ionizing radiation (IR) or oxidative damage (Ditch and Paull, 2012; Shiloh, 2014). More recently, increasing evidence has demonstrated that ATM plays critical functions in protein synthesis and degradation (Santini et al., 2014; Yang and Kastan, 2000), mitochondria ATP generation, reactive oxygen species (ROS) production and cellular respiration (Ambrose et al., 2007; Valentin-Vega et al., 2012).

Recent works in skeletal muscle-derived cells and soleus muscle have demonstrated that cytoplasmic ATM is involved in the insulin/IGF-1 signaling cascade by phosphorylating Akt family proteins (Andrisse et al., 2013; Ching et al., 2013; Jeong et al., 2010). However, to our knowledge, no information has been reported on the role of ATM in skeletal muscle structure and function.

Based on the current data, we hypothesized that the absence of central nervous system neurodegeneration in *Atm*-knockout ($Atm^{-/-}$) mice could allow the specific investigation of potential primary skeletal muscle and peripheral nervous system defects.

Here, we show, for the first time, a defective skeletal muscle phenotype in $Atm^{-/-}$ mice. The lack of Atm was sufficient to induce severe muscle wasting and atrophy associated with significant alteration of sarcomere organization, and significant changes in mitochondria number, morphology and ROS production. Analysis

[1]Department of Anatomical, Histological, Forensic and Orthopaedic Sciences, Sapienza University, 00161 Rome, Italy. [2]Department of Oncohaematology, IRCCS Ospedale Pediatrico Bambino Gesù, 00165 Rome, Italy. [3]Department of Biomedicine and Prevention, Tor Vergata University, 00133 Rome, Italy. [4]Institute of Cell Biology and Neurobiology, CNR, Monterotondo, 00015 Rome, Italy. [5]Epigenetics and Neurobiology Unit, European Molecular Biology Laboratory (EMBL), Monterotondo, 00015 Rome, Italy.
*These authors contributed equally to this work

‡Author for correspondence (manuela.pellegrini@cnr.it)

V.D.G., 0000-0002-6515-7637; M.P., 0000-0003-3348-5297

Received 20 July 2018; Accepted 22 January 2019

Journal of Cell Science (2019) 132, jcs223008. doi:10.1242/jcs.223008

of phosphoinositide 3-kinase (PI3K)/Akt signaling cascade revealed activation of several atrophy-related genes, inhibition of autophagic pathways and reduction of protein synthesis complex. Metabolic assay showed a switch to oxidative fibers, and biochemical and molecular analyses highlighted an increase of the myosin structural component of the skeletal muscle. Neuromuscular junctions were also affected in $Atm^{-/-}$ mice, according to morphological and molecular investigations. In summary, we show that the $Atm^{-/-}$ model is valuable to study the impact of Atm in skeletal muscle homeostasis and to investigate the intracellular signal perturbations following Atm impairment.

RESULTS

Atm$^{-/-}$ mice exhibit reduced muscle mass and fiber size

$Atm^{-/-}$ males and females show smaller size and reduced body weight compared to $Atm^{+/+}$ mice (Barlow et al., 1996; Di Siena et al., 2018; Elson et al., 1996) (Fig. 1A,B). We isolated and weighed individual muscles from males, such as the slow twitch soleus, the mixed tibialis anterior and the mixed quadriceps. All the muscles dissected from $Atm^{-/-}$ males showed a significant mass reduction compared to those from $Atm^{+/+}$ mice (Fig. 1C). We next evaluated the consequence of Atm deficiency by H&E staining of sections from soleus (Fig. 1D). The number of fibers was similar in solei of $Atm^{+/+}$ and $Atm^{-/-}$ mice (Fig. 1E). Although no necrotic and degenerating fibers were found in $Atm^{-/-}$ mice, myofibers appeared extremely small compared to those in $Atm^{+/+}$ controls (Fig. 1D). Quantification of fiber area reveals that there was an increased number of hypotrophic fibers in $Atm^{-/-}$ solei [Fig. 1F; mean cross sectional area (CSA) values: $Atm^{+/+}$, 1153.27±93.65; $Atm^{-/-}$, 477.55±129.33].

Collectively, these data indicate that absence of Atm kinase severely affects muscle mass, primarily by decreasing myofiber size.

Increase of muscle atrophy in *Atm*$^{-/-}$ tibialis anterior

Expression of atrophy-related genes was then investigated. The most critical players in muscle atrophy are the transcription factors of the forkhead box O (FoxO) family (Sandri et al., 2004). The dephosphorylation/activation of FoxO3 leads to upregulation of MAFbx (also known as Atrogin1 or FBXO32) and MuRF1 (also known as TRIM63), which represent molecular targets of FoxO activity (Sandri et al., 2004; Schiaffino et al., 2013). Western blot analysis revealed a selective downregulation of the phosphorylated form of FoxO3 in $Atm^{-/-}$ compared to $Atm^{+/+}$ mice (Fig. 2A). This was accompanied by autophagy inhibition, as measured by the decrease in the ratio of LC3-II:LC3-I (Fig. 2A), which has been reported to cause muscle atrophy (Mammucari et al., 2007). Quantitative RT-PCR (qRT-PCR) analysis revealed that both *MuRF1* and *Atrogin1* expression is increased in $Atm^{-/-}$ compared to $Atm^{+/+}$ mice (Fig. 2B). Taken together, these results indicate that Atm is indispensable for skeletal muscle integrity by inducing autophagic pathways and inhibiting atrophy-related genes.

Impairment of Akt pathway and protein synthesis in *Atm*$^{-/-}$ tibialis anterior

Muscle atrophy might be related to an increase of protein degradation through activation of the proteasome–ubiquitin pathway (Bilodeau et al., 2016; Santini et al., 2014) and/or to defects in protein synthesis (Yang and Kastan, 2000).

We initially analyzed the ubiquitin–proteasome pathway in protein extracts derived from tibialis anterior muscles. Western blot analysis revealed that total protein ubiquitylation is not significantly increased in $Atm^{-/-}$ compared to $Atm^{+/+}$ tibialis anterior muscle (data not shown).

A-T patients show reduced IGF-1 serum level, and decreased Akt phosphorylation has been observed in several ATM-deficient systems indicating a compromised IGF-1–PI3K–Akt axis and defective protein synthesis process in the absence of ATM. In order to study whether an impairment of Akt pathway could be correlated with muscle wasting in $Atm^{-/-}$ mice, protein extracts from tibialis anterior of wild-type and knockout mice were analyzed for phosphorylation of Akt family proteins and for the activation state of translation complexes (Fig. 3). Akt phosphorylation was strongly reduced in tibialis from $Atm^{-/-}$ mice and also the phosphorylated form of its target GSK3β (Fig. 3A,B). Notably, a decreased phosphorylation was observed for the cap-binding factor eIF4E and for the eIF4E-binding protein, 4E-BP1 (also known as EIF4EBP1) (Fig. 3A,B). These results suggest that Atm is indispensable for skeletal muscle protein synthesis through the PI3K/Akt pathway.

Increased number of oxidative myofibers and upregulation of slow myosin in *Atm*$^{-/-}$ mice

To investigate whether fiber atrophy was associated to a metabolic alteration, we performed NADH-tetrazolium reductase (NADH-TR) staining on frozen sections of tibialis anterior. $Atm^{-/-}$ muscles displayed increased prevalence of oxidative fibers at the expense of glycolytic fibers, which display decreased numbers (Fig. 4A). Since abundance of oxidative fibers is typically associated with type I fiber predominance, the levels of myosin heavy chain (MyHC) of the slow type was assayed by immunofluorescence staining. Slow MyHC is barely expressed in $Atm^{+/+}$ tibialis anterior; however, a strong increase of the myosin was detected in $Atm^{-/-}$ tibialis (Fig. 4B). These results were confirmed by western blot analysis (Fig. 4C), which showed that also total MyHC protein levels were increased in $Atm^{-/-}$, suggesting a global upregulation of myosin isoforms. A detailed analysis of myosin transcripts revealed that both mRNAs for slow MyHC1 (encoded by *Myh7*) and those of the fast type, MyHC2A and MyHC2B (encoded by *Myh2* and *Myh4*) were significantly increased in $Atm^{-/-}$ compared to $Atm^{+/+}$ soleus muscle (Fig. 4D).

Collectively, these data suggest increased oxidative fiber abundance in the absence of Atm, with a significant fast-to-slow fiber-type switching.

Abnormal muscle architecture and elevated mitochondrial ROS production in *Atm*$^{-/-}$ muscle

Tibialis anterior of $Atm^{+/+}$ and $Atm^{-/-}$ mice was analyzed at ultrastructural level by transmission electron microscopy (TEM) (Fig. 5). We observed several morphological abnormalities in $Atm^{-/-}$ muscles. The most evident alterations were the increased number and size of coupled mitochondria present at the Z-lines in the muscle of $Atm^{-/-}$ (Fig. 5E,I) compared to $Atm^{+/+}$ (Fig. 5A,I) mice. In several cases, mitochondria were clustered in longitudinal rows between myofibrils, appearing abnormally shaped and sized (Fig. 5E) and, rarely, swollen (Fig. 5F,G) in $Atm^{-/-}$ (Fig. 5F,G) compared to $Atm^{+/+}$ tibialis (Fig. 5B,C).

Myofibrillar architecture appeared normal, although sarcomeres were often out of register in $Atm^{-/-}$ (Fig. 5E, black asterisks) compared to $Atm^{+/+}$ tibialis (Fig. 5A). Sarcomeric units were found in overabundance, with shorter Z-lines in $Atm^{-/-}$ (Fig. 5E,I) compared to $Atm^{+/+}$ (Fig. 5A,I) mice, despite their similarity in length (Fig. 5I). No abnormalities were noted in triad structure (Fig. 5C,G), which were normally flanking each Z-line at the myofibril border. These data indicate that $Atm^{-/-}$ skeletal muscles

Journal of Cell Science (2019) 132, jcs223008. doi:10.1242/jcs.223008

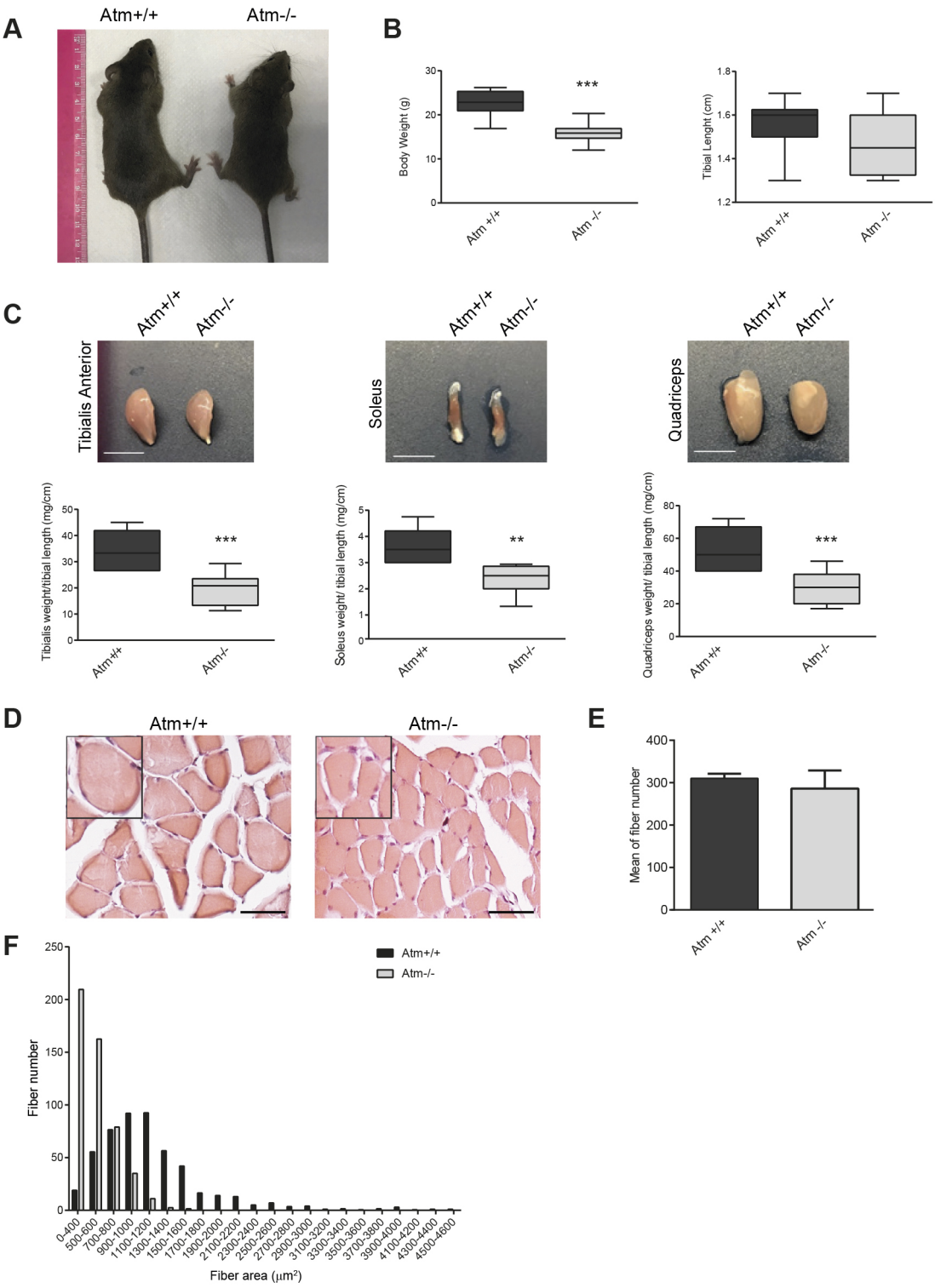

Fig. 1. Morphometry of skeletal muscles in *Atm*$^{-/-}$ mice. (A) Representative images of 2-month-old males showing the reduced size of *Atm*$^{-/-}$ mice. (B) Body weight and tibia length are reported for 2-month-old *Atm*$^{+/+}$ and *Atm*$^{-/-}$ mice. *n*=10 mice/genotype. ***P<0.001. (C) Representative image of tibialis anterior, soleus and quadriceps muscles and relative weight from 2-month-old *Atm*$^{+/+}$ and *Atm*$^{-/-}$ mice. *n*=7 mice/genotype. Scale bars: 0.5 cm. **P<0.01; ***P<0.001. The box represents the 25–75th percentiles, and the median is indicated. The whiskers show the minimum and maximum values. (D) H&E staining of a soleus section from *Atm*$^{+/+}$ and *Atm*$^{-/-}$ mice. Scale bars: 50 µm. Magnification of fibers and nuclei are shown in the insets. (E) Count of fiber number in solei of *Atm*$^{+/+}$ and *Atm*$^{-/-}$ mice. The mean±s.e.m. value is reported. *n*=3 mice/genotype. (F) Frequency distribution of soleus fiber size from *n*=2 mice for each genotype. The CSA of most soleus fibers ranged between 100 and 400 µm^2 in *Atm*$^{-/-}$ mice.

present ultrastructural defects both in the contractility machinery and in the organelles that produce cellular energy, suggesting an increase of ROS and a defective oxidative stress response in *Atm*$^{-/-}$ muscles. For this reason, mitochondrial superoxide production was evaluated by MitoSOX Red fluorogenic dye in freshly isolated tibialis anterior muscles (Fig. 6) of *Atm*$^{+/+}$ and *Atm*$^{-/-}$ mice. As

Journal of Cell Science (2019) 132, jcs223008. doi:10.1242/jcs.223008

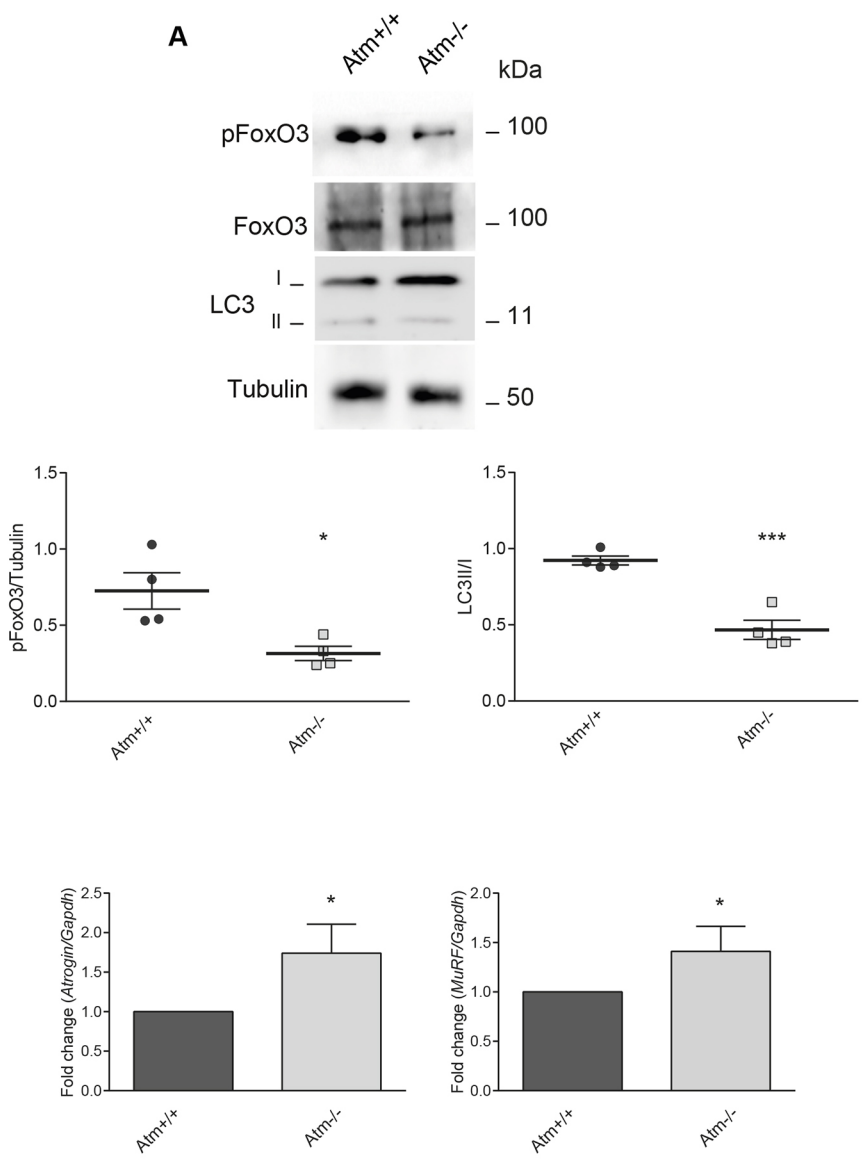

Fig. 2. Molecular signature of atrophy increases and autophagy decreases in *Atm*$^{-/-}$ skeletal muscles. (A) Representative western blot for a marker of atrophy (FoxO3a) and of autophagy (LC3) as revealed in proteins extracted from tibialis anterior muscle of *Atm*$^{+/+}$ and *Atm*$^{-/-}$ mice. Densitometric quantification shows a decrease of FoxO3a phosphorylation (pFoxO3) and a decrease of LC3-II:LC3-I ratio in *Atm*$^{-/-}$ compared to *Atm*$^{+/+}$ tibialis anterior muscles. Dot plots of individual data points and mean±s.e.m. values are shown. FoxO3a and tubulin were used as loading control. n=4 mice/genotype. *P<0.05; ***P<0.001. (B) qRT-PCR analysis of the FoxO3 targets *Atrogin1* and *MuRF1* confirming the activation of atrophic pathways in *Atm*$^{-/-}$ skeletal muscles. *Gapdh* was used as a housekeeping gene. Data were obtained from triplicates of n=3 mice/genotype. *P<0.05. The mean±s.e.m. values are reported.

shown in Fig. 6A,B, the relative fluorescence intensity of MitoSOX Red in muscle fibers of *Atm*$^{-/-}$ mice is significantly higher when compared to *Atm*$^{+/+}$ muscle fibers.

Neuromuscular junction defects in *Atm*$^{-/-}$ muscle

The ability to form and maintain synapses is a fundamental property of the mammalian nervous system required to generate functional neuromuscular connection and to establish a network connectivity. The size, shape and complexity of synapses were evaluated in quadriceps of *Atm*$^{+/+}$ and *Atm*$^{-/-}$ mice by staining with α-bungarotoxin and PGP 9.5 or synaptophysin 1 to monitor the muscular and nervous counterparts of the neuromuscular junction, respectively (Chen et al., 2010) (Fig. 7A,C and data not shown). Analyses of α-bungarotoxin immunofluorescence (Fig. 7A) revealed no alteration in the number of neuromuscular junctions (NMJs) in *Atm*$^{-/-}$ compared to *Atm*$^{+/+}$ mice (Fig. 7B), while the area of NMJs was increased, as well as the total length and average number of NMJ branches (Fig. 7A,B) in *Atm*$^{-/-}$ muscles. We found that the number of secondary branches was increased in *Atm*$^{-/-}$ tibialis anterior and both primary and secondary branches showed increased length (Fig. 7A,B). Overlapping staining of α-bungarotoxin and PGP 9.5 or synaptophysin 1 of NMJ suggests muscle-specific defects without synaptic transmission impairment in *Atm*$^{-/-}$ mice (Fig. 7C and data not shown). We further investigated the expression of the α7 neuronal nicotinic acetylcholine receptor subunit and myogenin, the transcription factor promoting acetylcholine receptor gene transcription. An increase of the receptor and its regulator was observed in solei from *Atm*$^{-/-}$ mice compared to *Atm*$^{+/+}$ mice (Fig. 7D,E). Taken together, these results indicate that the complexity of NMJ is increased in *Atm*$^{-/-}$ mice, possibly reflecting the switch to oxidative fibers.

DISCUSSION

Mutations in the human *ATM* gene, located on the long arm of chromosome 11 (q22–23), cause A-T, a highly pleiotropic autosomal recessive disorder (Platzer et al., 1997; Savitsky et al., 1995). A-T patients exhibit hematologic malignancy, neurodegeneration, sterility and radiosensitivity (Lavin and Shiloh, 1997). A-T patients are also characterized by growth retardation, heart problems, tremors and several difficulties in movements; however, it is not possible to distinguish whether muscle defects are secondary to the cerebellar defects or primary to muscle fibers. Here, we report a novel

Journal of Cell Science (2019) 132, jcs223008. doi:10.1242/jcs.223008

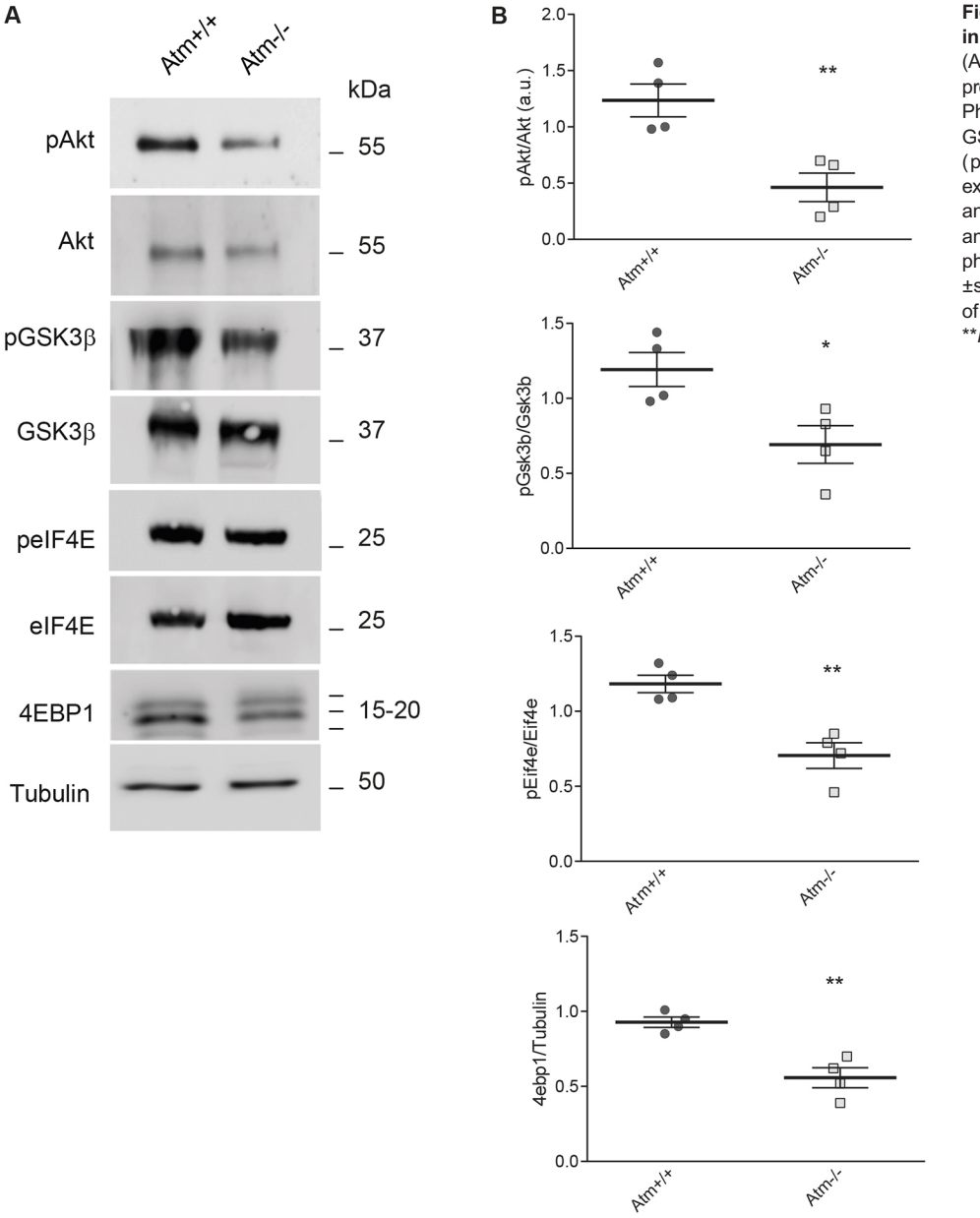

Fig. 3. Protein synthesis impairment in muscles from *Atm*$^{-/-}$ mice.
(A) Representative western blot of the protein targets downstream of Atm kinase. Phosphorylated Akt (pAkt), phosphorylated GSK3β (pGSK3β), phosphorylated eIF4E (peIF4E) and 4E-BP1 were monitored in extract from tibialis anterior muscle of *Atm*$^{+/+}$ and *Atm*$^{-/-}$ mice. (B) Relative densitometric analysis of phosphorylated versus non-phosphorylated protein is reported as mean ±s.e.m value of n=4 mice/genotype. Dot plots of individual data points are shown. *P<0.05, **P<0.01.

phenotype of *Atm*$^{-/-}$ mice related to severe skeletal muscle defects at structural and signaling levels that might impair muscle functionality.

Despite neuromotor defects and neurological abnormalities, *Atm*$^{-/-}$ mice do not develop central nervous system defects and do not manifest neurodegeneration, presumably because they die early (Barlow et al., 1996; Elson et al., 1996; Kuljis et al., 1997). For these reasons, the *Atm*$^{-/-}$ model allows study of primary skeletal muscle and neuromuscular junction defects. Our analysis revealed that almost 80% of male mice showed reduced body weight; in addition, various skeletal muscles analyzed showed that they were smaller in size compared to those in wild-type litters. Further analysis in soleus muscles showed that fiber number was unaltered but cross sectional area was reduced more than 2-fold in *Atm*$^{-/-}$ mice. In A-T patients, GH/IGF-1 blood serum levels are often reduced (Kieslich et al., 2010), partially explaining patient body weight reduction. Given the high variability among mice, we did not obtain conclusive results on *Igf1* transcript levels in soleus muscle from *Atm*$^{-/-}$. Nevertheless, a clear inhibition of the PI3K/Akt pathway was observed in tibialis anterior muscles, consistent with previous reports describing that Atm kinase is crucial for Akt phosphorylation and protein translation (Jeong et al., 2010; Yang and Kastan, 2000). Moreover, genes related to atrophy were upregulated through FoxO3a-mediated protein de-phosphorylation. The autophagic pathway, as monitored by the ratio between the two LC3 forms that are differently phospholipidated, was reduced in *Atm*$^{-/-}$ muscles as was previously reported in the absence of its kinase activity (Santini et al., 2014), suggesting a defect in the turnover of muscle fibers in this mouse model and supporting the normal number of fibers observed in muscles.

Investigation of the myosin component revealed an increase of slow myosin that correlated with a switch to slow-twitched fibers in *Atm*$^{-/-}$ muscle. However, an increase of MyHC2A and MyHC2B was also observed, contributing to the amount of total myosin detected by western blot. A possible explanation of total myosin protein upregulation and fiber atrophy is the increase of sarcomere number, as observed at the electron microscopy, in *Atm*$^{-/-}$

Journal of Cell Science (2019) 132, jcs223008. doi:10.1242/jcs.223008

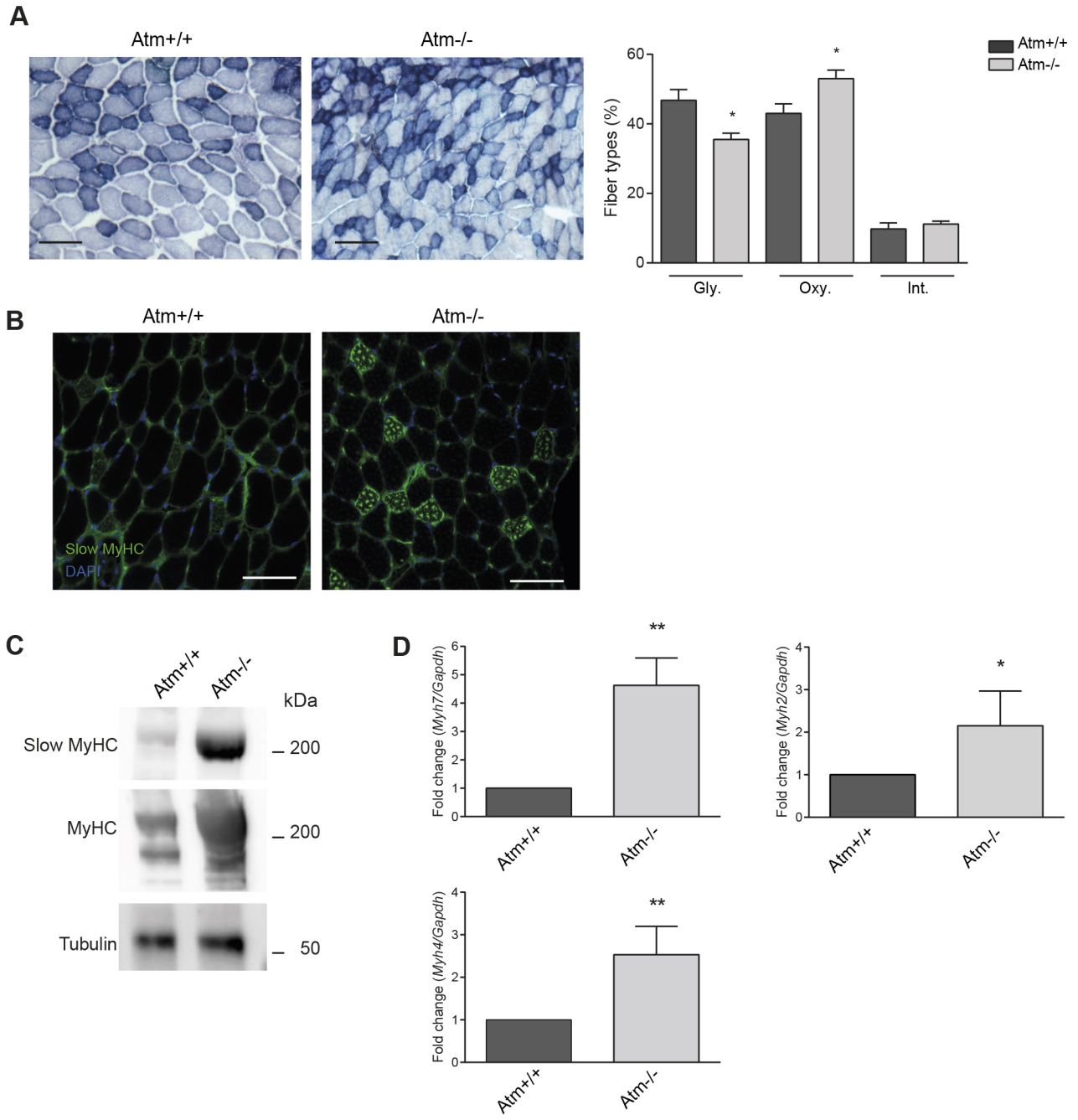

Fig. 4. *Atm*$^{-/-}$ mice exhibited increased numbers of oxidative myofibers and induction of myosin isoform expression. (A) NADH-TR staining of tibialis anterior muscle sections. Quantitative analysis was performed in tibialis anterior sections from *n*=4 mice/genotype. Scale bar: 100 µm. Fibers were classified as glycolytic (Gly., white), intermediate (Int., light blue) or oxidative (Ox., dark blue) based on staining intensity. (B) Representative immunofluorescence staining of slow MyHC (green) in tibialis anterior muscle of *Atm*$^{+/+}$ and *Atm*$^{-/-}$. The sarcolemma is visible by the unspecific staining of anti-slow MyHC antibody. Nuclei were stained with DAPI. Scale bar: 100 µm. (C) Representative western blot analysis of protein extracts obtained from tibialis anterior muscles. Slow and total MyHC increased in the *Atm*$^{-/-}$ muscles. Tubulin was used as loading control. Data were obtained from *n*=4 mice/genotype of each genotype. (D) qRT-PCR analysis of MyHC1 (*Myh7*), and MyHC2A and MyHC2B (*Myh2 and Myh4*) isoforms. *Gapdh* was used as housekeeping gene. Data were obtained from triplicates of *n*=4 mice/genotype. *P<0.05, **P<0.01. The mean±s.e.m. values are reported in A and D.

compared to *Atm*$^{+/+}$ muscle. This result might suggest that more contraction modules and, consequently more myosin molecules, are required in *Atm*$^{-/-}$ muscles, possibly due to functional compensatory effects. The most notable alteration observed in the ultrastructural organization of *Atm*$^{-/-}$ muscle fibers was the enlargement of coupled mitochondria, their higher number and the presence of giant mitochondria that might be correlated to premature aging of *Atm*$^{-/-}$ mouse models. Mitochondrial morphological alterations were previously observed in thymocytes from *Atm*$^{-/-}$ mice (Valentin-Vega et al., 2012) and they were related to an increase of ROS levels, a reduction in ATP production and oxidative complex I deficiency in these cells (Stagni et al., 2018; Valentin-Vega et al., 2012). Indeed, evaluation of ROS revealed increased levels of superoxide in the mitochondria of live fibers of *Atm*$^{-/-}$

Journal of Cell Science (2019) 132, jcs223008. doi:10.1242/jcs.223008

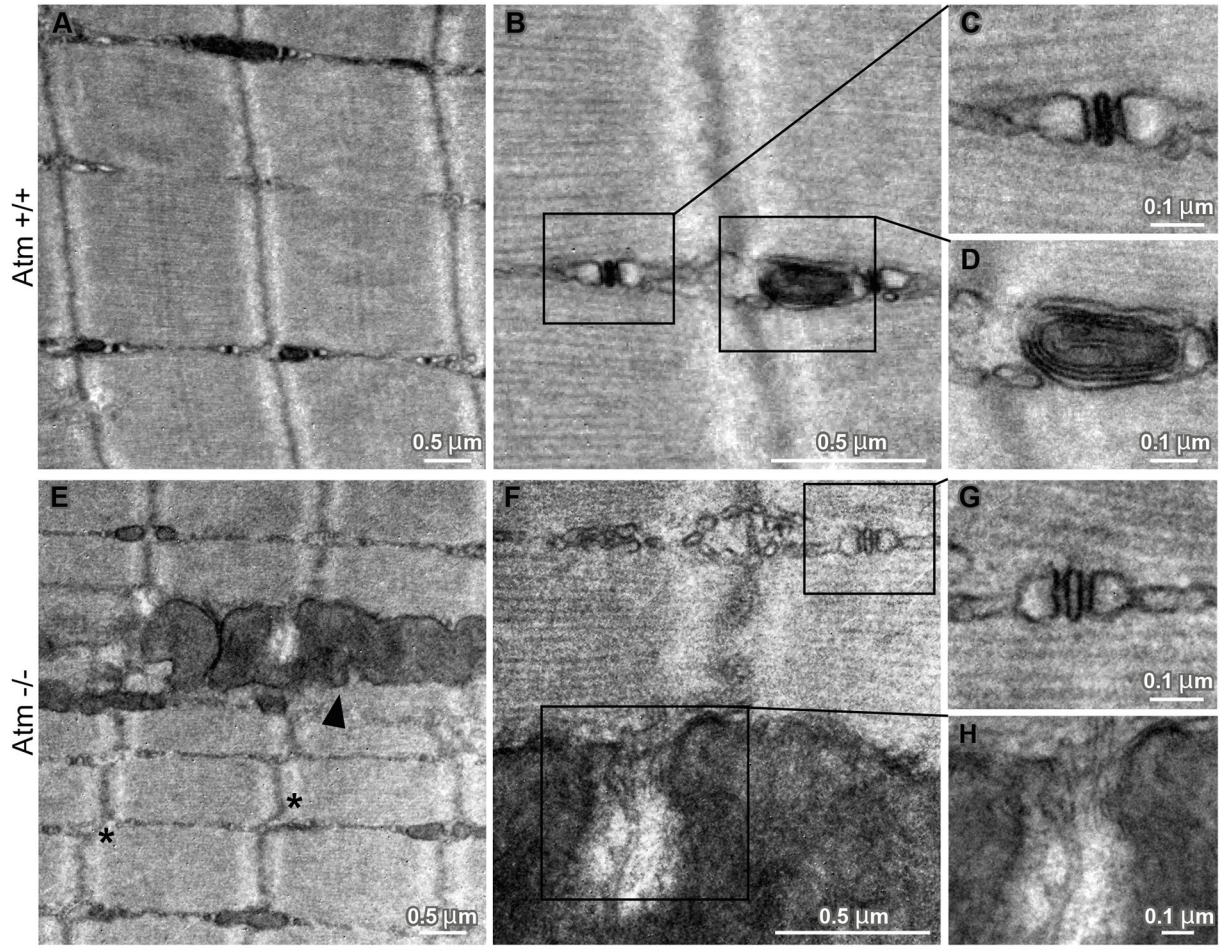

I

Morphological features	*Atm+/+*	*Atm-/-*
n. of sarcomeres/column/47µm^2	5.66 ± 0.33	7.66 ± 0.33*
Sarcomere length long axis (µm)	1.84 ± 0.06 (49)	1.9 ± 0.05 (41)
Sarcomere length short axis (µm)	1.13 ± 0.08 (49)	0.81 ± 0.05*(41)
n. of coupled mitochondria/47 µm^2	8 ± 2.51	18.33 ± 1.45*
Average diameter of coupled mitochondria (nm)	299.3 ± 16.58 (261)	385.3 ± 21.88*(399)

Values are means ± sem.
In parenthesis number of sarcomeres and mitochondria analyzed.
* indicates significant difference between *Atm* $^{+/+}$ and *Atm* $^{-/-}$ groups. *P<0.05.

Fig. 5. Abnormal myofibrillar architecture in the absence of Atm. (A–H) TEM micrographs of tibialis anterior muscle from $Atm^{+/+}$ and $Atm^{-/-}$ mice. Control mice exhibited normal myofibrillar architecture (A,D). $Atm^{-/-}$ compared to $Atm^{+/+}$ muscles showed an increased number of sarcomeres per area unit (A versus E,I), shorter Z-lines (A versus E,I), and an increased number and diameter of coupled mitochondria. Giant mitochondria (A versus E), swollen and with disorganized cristae (B,D versus F,H) were also observed. Asterisks indicate out of register Z-lines. The black arrowhead indicates a giant mitochondrion. Data were obtained from *n*=3 mice/genotype. Different magnifications are shown and scale bar sizes are indicated.

mice compared to the age matched wild-type controls, implying that ATM could guarantee muscle integrity.

To understand whether ultrastructural alteration would be reflected in periphery nervous system defects, we analyzed neuromuscular junctions, because they represent a functional bridge between the muscle and nervous compartments. Increase of α7 nicotinic acetylcholine receptor levels and increase of NMJ surface area and complexity of branching implicate dysfunctional plaques in $Atm^{-/-}$ muscles, and correlate with type fiber switching and aging in $Atm^{-/-}$ mice. Nevertheless, no alteration was evident in terminal nerves as evaluated by synapse and synaptic vesicles marker staining. Indeed, recent works have demonstrated that muscle-specific defects influence NMJ integrity despite preserved central nervous system (Dobrowolny et al., 2018, 2008).

Overall, considering the latest and previous defects together with the heart skeletal muscle problems reported in humans, we might hypothesize alteration in muscle contraction and function in the absence of ATM. In the future, we will address the functionality of skeletal muscle fibers isolated from $Atm^{-/-}$ mice in physiological conditions and after skeletal muscle damage.

In summary, these results clearly indicate that $Atm^{-/-}$ mouse model shows skeletal muscles defects at the tissue, cellular and

Journal of Cell Science (2019) 132, jcs223008. doi:10.1242/jcs.223008

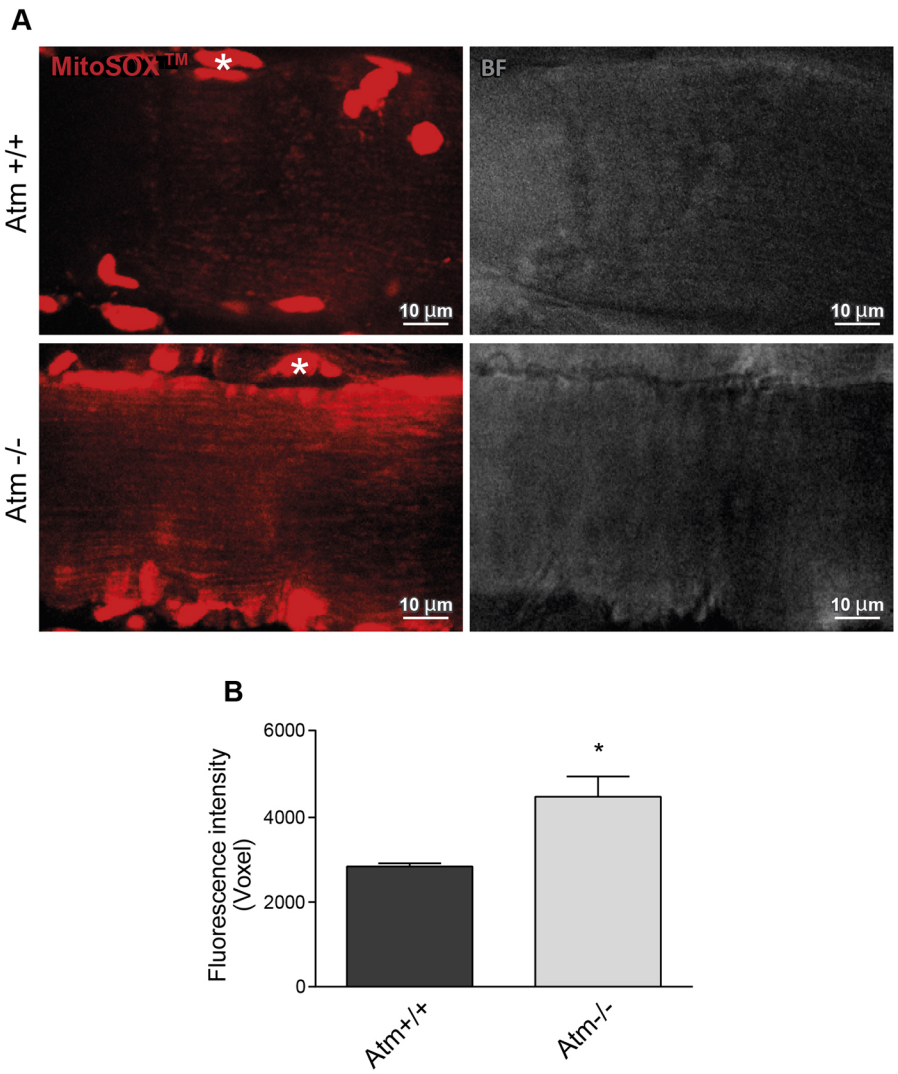

Fig. 6. Increased ROS levels in live tibialis anterior muscles of *Atm*$^{-/-}$ mice. (A) Representative maximum intensity projections of live *Atm*$^{+/+}$ and *Atm*$^{-/-}$ fibers stained with MitoSOX Red (left panels, red) and relative bright field (right panels, BF). White asterisks indicate unspecific staining of cell nuclei. (B) Fluorescence intensity analysis of MitoSOX Red labeling in *Atm*$^{+/+}$ and *Atm*$^{-/-}$ mice is measured in voxel units. Data are mean±s.e.m. obtained from *n*=3 mice/genotype. **P*<0.05.

ultrastructural levels. The muscle phenotype of *Atm*$^{-/-}$ mice is more relevant if considering that most of A-T patients die because of defects in diaphragm contraction and respiratory failure. In this context, our data showing that *Atm*$^{-/-}$ mice manifest skeletal muscle defects provide support for multisystem therapeutic interventions restoring ATM function in nervous and skeletal muscle ATM-deficient cells and promote future studies into the role of ATM in oxidative stress, atrophy and aging.

MATERIALS AND METHODS

Mice

Atm$^{+/-}$ mice, previously generated (Barlow et al., 1996), were kindly provided by Andre Nussenzweig (National Institutes of Health, Baltimore, MD). For experimental analysis were used males of 2 months of age in 129/SvEv×C57BL/6J background, obtained from the following breeding: *Atm*$^{+/-}$×*Atm*$^{+/-}$.

The following primers were used for genotyping: Atm-F, 5′-GACTTC-TGTCAGATGTTGCTGCC-3′; Atm-R, 5′-CGAATTGCAGGAGTTGCT-GAG-3′; Atm-Neo, 5′-GGGTGGGATTAGATAAATGCCTG-3′ Atm-F/R identifies the wild-type allele (200 bp) and Atm-F/Neo identifies the null allele (400 bp).

The health status of the treated mice was monitored twice a week. Mice were housed at the animal facility of Tor Vergata University, under standard conditions with free access to food diet and water. All animal studies were performed in accordance with the Guidelines for the Care and Use of Laboratory Animals and protocols were approved by the Tor Vergata Animal Care, Ethics Committee and the Italian Ministry of Health (protocol no. 1104/2016-PR, art. 31 of D.lgs 24/2014).

Tissue isolation

Mice were weighed in a technical scale (VWR, Science Education). After cervical dislocation, muscles were immediately dissected and weighed in pairs using an analytical scale (Ohaus Pioneer). For mRNA and protein extraction, tissues were snap-frozen in cold-ice and stored at −80°C. For hematoxylin and eosin (H&E) staining, tissue was fixed overnight in formalin (Sigma). For immunofluorescence and NADH-TR staining, muscles were snap-frozen in liquid-nitrogen-cooled isopentane and stored at −80°C until cryosectioning. For neuromuscular junction detection, quadriceps were embedded in OCT (Bio-Optica), snap-frozen in liquid-nitrogen-cooled isopentane and stored at −80°C until preparation of cryosections.

Skeletal muscle histological analysis, CSA measurement and immunofluorescence

Immediately after animals were euthanized, the two gastrocnemius, soleus and tibialis anterior muscles, were dissected and weighed. Tibialis and soleus were used to perform the molecular and histological analysis. Muscles used for histology were immediately fixed in 10% phosphate-buffered formalin and embedded in paraffin. The morphological changes were measured by H&E staining of 5 µM sections following standard procedures. Myofiber cross sectional area (CSA) measurement was performed on paraffin-embedded soleus from *Atm*$^{+/+}$ and *Atm*$^{-/-}$ mice.

Journal of Cell Science (2019) 132, jcs223008. doi:10.1242/jcs.223008

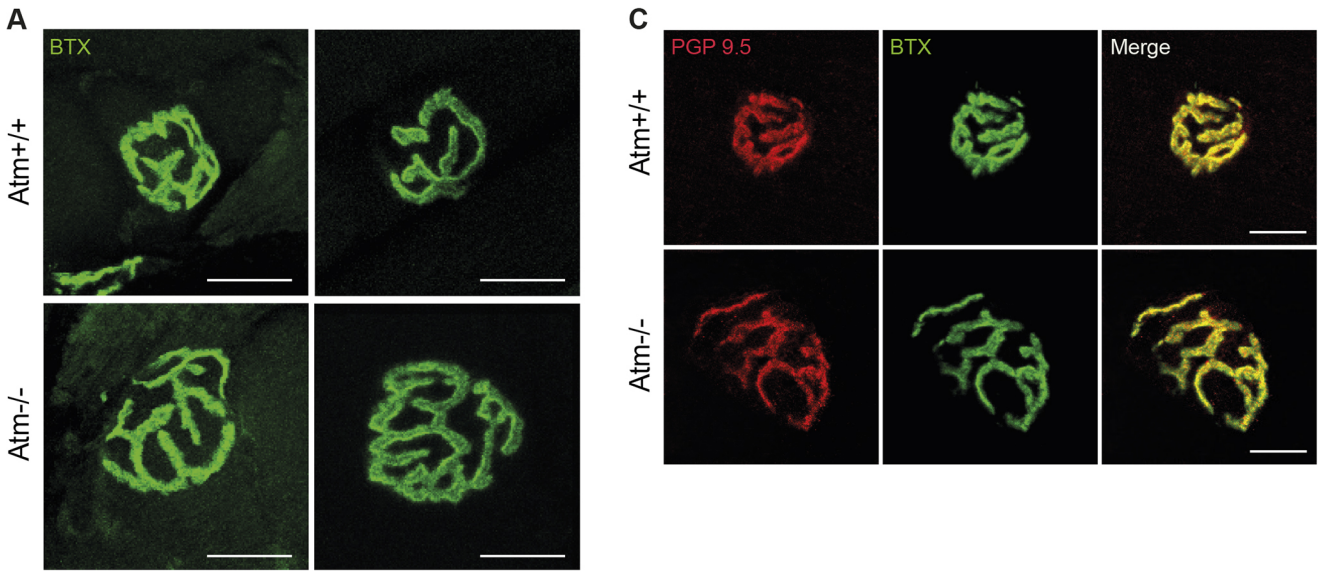

B

Morphometric analyses of NMJ	*Atm+/+ (n=11)*	*Atm-/- (n=11)*
Planar area (μm^2)	471.30 ± 55.97	637.62 ± 34.94*
Number of NMJ / cluster	13.64 ± 2.87	12.64 ± 3.36
Total length of branches / NMJ (μm)	110.25 ± 8.23	161.15 ± 16.79*
Average length of branches / NMJ (μm)	16.49 ± 0.98	17.19 ± 1.41
Average no of branches / NMJ	6.91 ± 0.67	10.09 ± 1.37*
Total length of 1° branches / NMJ (μm)	72.95 ± 5.23	101.12 ± 11.23*
Average lenght of 1° branches (μm)	31.53 ± 3.81	36.62 ± 2.92
Average number of 1° branches / NMJ	2.55 ± 0.26	2.82 ± 0.28
Total length of 2° branches / NMJ (μm)	37.30 ± 4.26	61.30 ± 10.44*
Average length of 2° branches (μm)	8.77 ± 0.69	8.92 ± 0.75
Average number of 2° branches / NMJ	4.36 ± 0.53	7.27 ± 1.27*

Values are means ± sem.
n indicates number of NMJ analyzed.
* Indicates significant difference between *Atm* $^{+/+}$ and *Atm* $^{-/-}$ groups. *P<0.05.

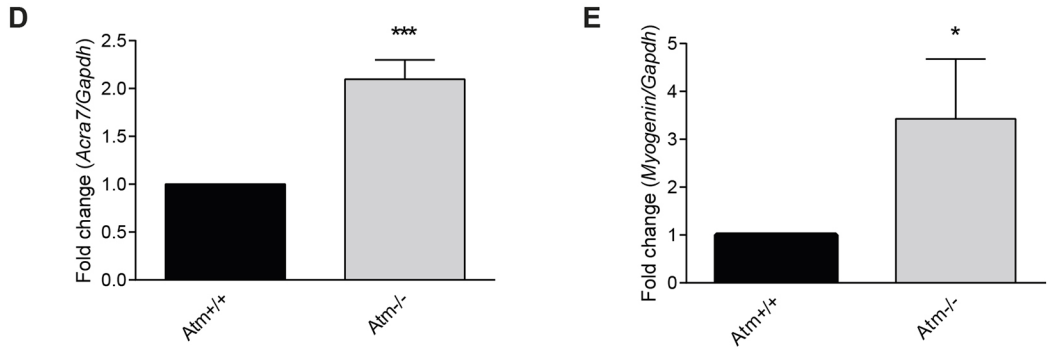

Fig. 7. See next page for legend.

Journal of Cell Science (2019) 132, jcs223008. doi:10.1242/jcs.223008

Fig. 7. NMJ abnormalities in *Atm*$^{-/-}$ muscles. (A) Representative maximum projection of micrographs showing α-bungarotoxin (BTX; green) staining in quadriceps muscles of *Atm*$^{+/+}$ (A) and *Atm*$^{-/-}$ (B) mice. Scale bars: 20 µm. (B) Morphometric analysis of quadriceps neuromuscular junctions. Analysis was performed in *n*=4 mice/genotype. (C) Representative maximum projection of photomicrographs showing α-bungarotoxin (green) and PGP 9.5 (red) staining in quadriceps muscles of *Atm*$^{+/+}$ and *Atm*$^{-/-}$ mice. Scale bars: 20 µm. (D,E) qRT-PCR analysis for α7 neuronal nicotinic acetylcholine receptor subunit (*Acra7*) and myogenin. *Gapdh* was used as housekeeping gene. Data are mean±s.e.m. obtained from triplicates of *n*=3 mice/genotype. **P*<0.05; ****P*<0.001.

Fifty serial muscle sections (8 µm) from the mid-portion to the distal-portion of each soleus were obtained and stained with H&E. Bright-field images were taken by using an Axioskop microscope (Carl Zeiss) and 10 fibers for each section were randomly selected and measured by using ImageJ software (version 1.49). For each slice, all the fibers were counted.

NADH-TR staining (Nitrotetrazolium Blue Chloride, N6876 and N6639, Sigma) was performed according to the manufacturer's protocol. Briefly, the oxidative reaction was conducted in 8 µm tibialis anterior cryosections incubated for 35 min at room temperature, washed with deionized water and mounted with Eukitt (Electron Microscopy Sciences). Images were acquired with an inverted microscope (Axiovert 200M; Carl Zeiss, Inc., Thornwood, NY). The number of oxidative, glycolytic and intermediate fibers was evaluated in three sections of *n*=4 mice/group.

Immunofluorescence staining was performed using standard protocols. After permeabilization and blocking with 1% BSA, samples were incubated with mouse anti-myosin, skeletal, slow (1:400, Sigma, #M8421) and diluted in 0.5% BSA overnight at 4°C. Secondary antibody anti-mouse-IgG conjugated to Alexa Fluor 488 was diluted 1:400. Images were acquired by Nikon Eclipse Ti-S microscope (Nikon Instruments, Nikon Instruments S.p.A, Firenze, Italy). DAPI was used to counterstain nuclei.

For NMJ staining, segments of quadriceps from *Atm*$^{+/+}$ and *Atm*$^{-/-}$ mice were embedded in OCT and snap-frozen in nitrogen-cooled isopentane.

Longitudinal frozen sections (40 µm) were fixed in paraformaldehyde 4% for 10 min and stained with polyclonal rabbit anti-PGP 9.5 (1:200, Dako, Z5116) or mouse anti-synaptophysin 1 antibody (1:50, Synaptic Systems, 101011) diluted in PBS with 3% BSA/5% donkey serum/0.05% Tween 20 overnight at 4°C and with α-bungarotoxin, Alexa Fluor 488 conjugate (1:1000, Invitrogen) at RT for 1 h. Alexa Fluor 555 (1:500) was used as secondary antibody. Slides were mounted with buffered glycerol 60% and confocal images were taken using an Olympus FV1200 laser scanning confocal microscope and analyzed with Olympus FluoView software. Images of at least 30 NMJ were taken for each group; the z-stacked fluorescence images (2 µm per focal plane) were collected and analyzed using ImageJ1.48p software (Wayne Rasband, National Institutes of Health).

The average number of NMJ per genotype was obtained by counting the junctions in 15 fields/mouse, randomly chosen, under a magnification of 20× objective. The analysis of the NMJ branches was performed according to previous reports (Prakash et al., 1996).

RNA isolation and qRT-PCR

Total RNA, from skeletal muscle tissues, was extracted with Trizol reagent and treated with DNase I (Ambion). DNA-free RNA was reverse transcribed using Promega cDNA Synthesis Kit according to the manufacturer's instructions.

qRT-PCR was performed with the SYBR-green master mix (Promega). Data were normalized to the level of *Gapdh* and fold change was determined by using the 2−ΔΔCT method. All reactions were performed in triplicate.

The following primers were used: Myh7 (MyHC1), Fw 5′-AGTCCCA-GGTCAACAAGCTG-3′ and Rv 5′-TTCCACCTAAAGGGCTGTTG-3′; Myh2 (MyHC2A), Fw 5′-AGTCCCAGGTCAACAAGCTG-3′ and Rv 5′-GCATGACCAAAGGTTTCACA-3′; Myh4 (MyHC2B), Fw 5′-AGTCC-CAGGTCAACAAGCTG-3′ and Rv 5′-TTTCTCCTGTCACCTCTCAAC-A-3′; Atrogin1, Fw 5′-AGCGCCATGGATACTGTACT-3′ and Rv 5′-TCAGCTCCAACAGCCTTACT-3′; MuRF1, Fw 5′-TGCAAGGAACAC-GAAGACGA-3′ and Rv 5′-TTTGCAAAGGGGCAACCTCA-3′; Igf1, Fw 5′-TGCTCTTCAGTTCGTGTG-3′ and Rv 5′-ACATCTCCAGTCTCCT-CAG-3′; myogenin, Fw 5′-TACAGACGCCCACAATCTGC-3′ and Rv 5′-AGTTGGGCATGGTTTCGTCT-3′; Acra7, Fw 5′-GCAGTGAGTGGA-AGTTTGCG-3′ and Rv 5′-GTTTGGGGCTGACATGAGGA-3′; and Gapdh, Fw 5′-GTGAAGGTCGGTGTGAACG-3′ and Rv 5′-ATTTGAT-GTTAGTGGGGTCTCG-3′.

Western blotting

For western blot analysis, protein extraction from tibialis anterior of *Atm*$^{+/+}$ and *Atm*$^{-/-}$ mice was performed in RIPA buffer (10 mM Tris-HCl pH 8.0, 140 mM NaCl, 1 mM EDTA, 0.5 mM EGTA, 1% Triton X-100, 0.1% sodium deoxycholate, 0.1% SDS, 0.5 M DTT, 100 mM PMSF, 1 M β-glycerophosphate, 0.5 M sodium orthovanadate and cocktail of protease inhibitors). Tissue desegregation was achieved with a Ultra-Turrax T25 homogenizer (Janke & Kunkel). Equal amounts from each lysate were separated in SDS polyacrylamide gel and transferred onto a nitrocellulose membrane (Amersham). The membrane was blocked in 1× Tris-buffered saline with 0.1% Tween 20/5% BSA for 1 h at room temperature and then filters were incubated with primary antibodies at 4°C overnight. Blots were washed extensively in 1× TBS-T and then incubated with the specific horseradish peroxidase-conjugated secondary antibody (Santa Cruz Biotechnology) for 1 h. The antibody binding was detected by chemiluminescence with an ECL kit (1:10,000, Santa Cruz Biotechnology) and images were recorded with the Syngene G-box system (Syngene Bioimaging, Haryana, India). Densitometric analyses were performed by ImageJ software (version 1.49). Antibodies used are listed below: mouse anti-tubulin (1:10,000, Sigma, T5168), mouse anti-ubiquitin (1:500, Santa Cruz Biotechnology, P4D1), rabbit anti-FoxO3a S253p (1:500, Cell Signaling, 9466), mouse anti-FoxO3a (1:500, Santa Cruz Biotechnology, 48348), rabbit anti-Akt S473p (1:1000, Santa Cruz Biotechnology, 7985), mouse anti-Akt (1:1000, Santa Cruz Biotechnology, 81434), rabbit anti-GSK3β S9p (1:1000, Cell Signaling, 9336), mouse anti-GSK3β (1:1000, Santa Cruz Biotechnology, 81462), rabbit anti-eIF4E S209p (1:1000, Invitrogen, 44-528G), mouse anti-eIF4E (1:1000, Santa Cruz Biotechnology, 271480), rabbit anti-4E-BP1 (1:1000, Cell Signaling, 9644), rabbit anti-LC3 (1:1000, MBL Int Corporation, PD014), mouse anti-myosin, skeletal, slow (1:400, Sigma, M8421), mouse anti-myosin heavy chain MyHC (1:5, from hybridoma bank, clone MF-20).

TEM

Tibialis anterior muscles were dissected from mice legs and immediately fixed with a mixture of 2% (w/v) PFA and 2.5% (w/v) glutaraldehyde (TAAB) in 0.1 M phosphate buffer (PB) pH 7.4 at 4°C for 24 h. Subsequently, samples were post-fixed with 1% (w/v) OsO_4 supplemented with 1.5% (w/v) potassium ferrocyanide for 1 h on ice, replaced by 1% (w/v) OsO_4 in sodium cacodylate 0.1 M for an additional hour. Samples were then dehydrated in series of ethanol and infiltrated with propylene oxide (Agar): Durcupan (Agar) (1:1) followed by Durcupan embedding for 48 h. Ultrathin sections were cut with an Ultracut S microtome (Leica), counter-stained with lead citrate and observed with a Jeol 1010 transmission electron microscope. Images were obtained using a Gatan MSC 791 CCD camera. The number of sarcomeres/column were evaluated in 30 images/genotype. The long and short axis, corresponding to I band distance and Z-line height, respectively, were evaluated in central sarcomeres of the image. The number of mitochondria were evaluated in 10 images/genotype. Dimensional analyses were performed with ImageJ software (version 1.49).

Live imaging of muscle fibers labeled with MitoSOX Red

Tibialis anterior muscles from 2-month-old mice were dissected longitudinally and labeled for 20 min at 37°C into HBSS buffer with 3.5 µM MitoSOX Red following (M36008 Invitrogen) manufacturer's instructions. Upon labeling, muscles were placed onto a 35 mm ø glass bottom dishes (Ibidi, Martinsried, Germany) and kept at constant temperature (37°C), humidity and CO_2 (5%) by using a microscope incubation chamber. Intact surfaces of tibialis were plated towards the detection lens (40× water) for direct imaging with a Spinning Disk confocal Ultraview Vox (Perkin Elmer), interfaced with Volocity 6.0 software (Cellular Imaging, Perkin Elmer). A solid state laser, operating at 488 nm was used as an excitation

source and a band pass emission filter-cube of 587 (W125) for the acquisition. Images were acquired using a Hamamatsu EMCCD camera; exposure time and camera sensitivity were the same for all samples.

Three-dimensional image analysis was carried out with the help of Imaris 8.0 (Bitplane). For each fiber at least two fixed volumes of 170×170 pixel (in *xy*) and 50 optical sections (in *z*) were measured as mean fluorescence intensity values. For both $Atm^{+/+}$ and $Atm^{-/-}$ mice a total of 20 random fibers were analyzed.

Statistical analyses

All data are expressed as mean±s.e.m. Samples from $Atm^{+/+}$ and $Atm^{-/-}$ were analyzed with Student's *t*-test, two tailed and one degree of freedom, and plotted by using Graph Pad Prism version 6.0 (Graph pad software). $P<0.05$ was considered significant for all tests.

Acknowledgements

We thank Dr Rossella Cicconi for technical assistance in the mouse colony maintenance and handling (Tor Vergata University, Rome, Italy); Dr Carmine Nicoletti, Dr Gabriella Dobrowolny, Laura Barberi and Dr Berghella Libera (Sapienza University, Rome, Italy) for helpful discussion and technical assistance in preparing tissue samples; Prof. Daniela Barilà (Tor Vergata University, Rome, Italy), Dr Linda Nocchi (EMBL, Monterotondo Scalo, Italy) and Prof. Antonio Musarò (Sapienza University, Rome, Italy) for reagent sharing.

Competing interests

The authors declare no competing or financial interests.

Author contributions

Conceptualization: M.P.; Methodology: V.T., V.D.G., G.L.S., G.B., L.D.A., M.P.; Validation: V.T., V.D.G., D.M.; Formal analysis: V.T., V.D.G., D.M., G.B., M.P.; Investigation: V.T., V.D.G., G.L.S., G.B.; Resources: M.P.; Data curation: V.T., V.D.G., G.L.S., D.M., M.P.; Writing - original draft: M.P.; Writing - review & editing: S.A., F.N., M.P.; Visualization: S.A., L.D.A.; Supervision: S.A., L.D.A., F.N., M.P.; Project administration: M.P.; Funding acquisition: F.N., M.P.

Funding

This work was supported by Ministero dell'Istruzione, dell'Università e della Ricerca [FIRB 2010: RBAP109BLT_003 to F.N., Ateneo 2016, 2017 to F.N., PRIN 2012: prot. 2012227FLF to M.P.].

References

Ambrose, M., Goldstine, J. V. and Gatti, R. A. (2007). Intrinsic mitochondrial dysfunction in ATM-deficient lymphoblastoid cells. *Hum. Mol. Genet.* **16**, 2154-2164.

Andrisse, S., Patel, G. D., Chen, J. E., Webber, A. M., Spears, L. D., Koehler, R. M., Robinson-Hill, R. M., Ching, J. K., Jeong, I. and Fisher, J. S. (2013). ATM and GLUT1-S490 phosphorylation regulate GLUT1 mediated transport in skeletal muscle. *PLoS ONE* **8**, e66027.

Barlow, C., Hirotsune, S., Paylor, R., Liyanage, M., Eckhaus, M., Collins, F., Shiloh, Y., Crawley, J. N., Ried, T., Tagle, D. et al. (1996). Atm-deficient mice: a paradigm of ataxia telangiectasia. *Cell* **86**, 159-171.

Bilodeau, P. A., Coyne, E. S. and Wing, S. S. (2016). The ubiquitin proteasome system in atrophying skeletal muscle: roles and regulation. *Am. J. Physiol. Cell Physiol.* **311**, C392-C403.

Browne, S. E., Roberts, L. J., Dennery, P. A., Doctrow, S. R., Beal, M. F., Barlow, C. and Levine, R. L. (2004). Treatment with a catalytic antioxidant corrects the neurobehavioral defect in ataxia-telangiectasia mice. *Free Radic. Biol. Med.* **36**, 938-942.

Chen, F., Sugiura, Y., Myers, K. G., Liu, Y. and Lin, W. (2010). Ubiquitin carboxyl-terminal hydrolase L1 is required for maintaining the structure and function of the neuromuscular junction. *Proc. Natl. Acad. Sci. USA* **107**, 1636-1641.

Ching, J. K., Luebbert, S. H., Collins, R. L., IV, Zhang, Z., Marupudi, N., Banerjee, S., Hurd, R. D., Ralston, L. and Fisher, J. S. (2013). Ataxia telangiectasia mutated impacts insulin-like growth factor 1 signalling in skeletal muscle. *Exp. Physiol.* **98**, 526-535.

Di Siena, S., Campolo, F., Gimmelli, R., Di Pietro, C., Marazziti, D., Dolci, S., Lenzi, A., Nussenzweig, A. and Pellegrini, M. (2018). Atm reactivation reverses ataxia telangiectasia phenotypes in vivo article. *Cell Death Dis.* **9**, 314.

Ditch, S. and Paull, T. T. (2012). The ATM protein kinase and cellular redox signaling: beyond the DNA damage response. *Trends Biochem. Sci.* **37**, 15-22.

Dobrowolny, G., Aucello, M., Rizzuto, E., Beccafico, S., Mammucari, C., Bonconpagni, S., Belia, S., Wannenes, F., Nicoletti, C., Del Prete, Z. et al. (2008). Skeletal muscle is a primary target of SOD1G93A-mediated toxicity. *Cell Metab.* **8**, 425-436.

Dobrowolny, G., Martini, M., Scicchitano, B. M., Romanello, V., Boncompagni, S., Nicoletti, C., Pietrangelo, L., De Panfilis, S., Catizone, A., Bouchè, M. et al. (2018). Muscle expression of $SOD1^{G93A}$ triggers the dismantlement of neuromuscular junction via PKC-theta. *Antioxid. Redox. Signal.* **28**, 1105-1119.

Elson, A., Wang, Y., Daugherty, C. J., Morton, C. C., Zhou, F., Campos-Torres, J. and Leder, P. (1996). Pleiotropic defects in ataxia-telangiectasia protein-deficient mice. *Proc. Natl. Acad. Sci. USA* **93**, 13084-13089.

Gatti, R. A., Shaked, R., Wei, S., Koyama, M., Salser, W. and Silver, J. (1988). DNA polymorphism in the human Thy-1 gene. *Hum. Immunol.* **22**, 145-150.

Hoche, F., Seidel, K., Theis, M., Vlaho, S., Schubert, R., Zielen, S. and Kieslich, M. (2012). Neurodegeneration in ataxia telangiectasia: what is new? what is evident? *Neuropediatrics* **43**, 119-129.

Jeong, I., Patel, A. Y., Zhang, Z., Patil, P. B., Nadella, S. T., Nair, S., Ralston, L., Hoormann, J. K. and Fisher, J. S. (2010). Role of ataxia telangiectasia mutated in insulin signalling of muscle-derived cell lines and mouse soleus. *Acta Physiol.* **198**, 465-475.

Kieslich, M., Hoche, F., Reichenbach, J., Weidauer, S., Porto, L., Vlaho, S., Schubert, R. and Zielen, S. (2010). Extracerebellar MRI—lesions in ataxia telangiectasia go along with deficiency of the GH/IGF-1 axis, markedly reduced body weight, high ataxia scores and advanced age. *Cerebellum* **9**, 190-197.

Kuljis, R. O., Xu, Y., Aguila, M. C. and Baltimore, D. (1997). Degeneration of neurons, synapses, and neuropil and glial activation in a murine Atm knockout model of ataxia-telangiectasia. *Proc. Natl. Acad. Sci. USA* **94**, 12688-12693.

Lavin, M. F. and Shiloh, Y. (1997). The genetic defect in ataxia-telangiectasia. *Annu. Rev. Immunol.* **15**, 177-202.

Lavin, M. F., Gueven, N., Bottle, S. and Gatti, R. A. (2007). Current and potential therapeutic strategies for the treatment of ataxia-telangiectasia. *Br. Med. Bull.* **81-82**, 129-147.

Mammucari, C., Milan, G., Romanello, V., Masiero, E., Rudolf, R., Del Piccolo, P., Burden, S. J., Di Lisi, R., Sandri, C., Zhao, J. et al. (2007). FoxO3 controls autophagy in skeletal muscle in vivo. *Cell Metab.* **6**, 458-471.

Micol, R., Ben Slama, L., Suarez, F., Le Mignot, L., Beauté, J., Mahlaoui, N., Dubois d'Enghien, C., Laugé, A., Hall, J., Couturier, J. et al. (2011). Morbidity and mortality from ataxia-telangiectasia are associated with ATM genotype. *J. Allergy Clin. Immunol.* **128**, 382-389.e1.

Platzer, M., Rotman, G., Bauer, D., Uziel, T., Savitsky, K., Bar-Shira, A., Gilad, S., Shiloh, Y. and Rosenthal, A. (1997). Ataxia-telangiectasia locus: sequence analysis of 184 kb of human genomic DNA containing the entire ATM gene. *Genome Res.* **7**, 592-605.

Prakash, Y. S., Miller, S. M., Huang, M. and Sieck, G. C. (1996). Morphology of diaphragm neuromuscular junctions on different fibre types. *J. Neurocytol.* **25**, 88-100.

Reliene, R., Fleming, S. M., Chesselet, M.-F. and Schiestl, R. H. (2008). Effects of antioxidants on cancer prevention and neuromotor performance in Atm deficient mice. *Food Chem. Toxicol.* **46**, 1371-1377.

Sandri, M., Sandri, C., Gilbert, A., Skurk, C., Calabria, E., Picard, A., Walsh, K., Schiaffino, S., Lecker, S. H. and Goldberg, A. L. (2004). Foxo transcription factors induce the atrophy-related ubiquitin ligase atrogin-1 and cause skeletal muscle atrophy. *Cell* **117**, 399-412.

Santini, S., Stagni, V., Giambruno, R., Fianco, G., Di Benedetto, A., Mottolese, M., Pellegrini, M. and Barilà, D. (2014). ATM kinase activity modulates ITCH E3-ubiquitin ligase activity. *Oncogene* **33**, 1113-1123.

Savitsky, K., Bar-Shira, A., Gilad, S., Rotman, G., Ziv, Y., Vanagaite, L., Tagle, D., Smith, S., Uziel, T., Sfez, S. et al. (1995). A single ataxia telangiectasia gene with a product similar to PI-3 kinase. *Science* **268**, 1749-1753.

Schiaffino, S., Dyar, K. A., Ciciliot, S., Blaauw, B. and Sandri, M. (2013). Mechanisms regulating skeletal muscle growth and atrophy. *FEBS J.* **280**, 4294-4314.

Schubert, R., Reichenbach, J. and Zielen, S. (2005). Growth factor deficiency in patients with ataxia telangiectasia. *Clin. Exp. Immunol.* **140**, 517-519.

Shiloh, Y. (2014). ATM: expanding roles as a chief guardian of genome stability. *Exp. Cell Res.* **329**, 154-161.

Stagni, V., Cirotti, C. and Barilà, D. (2018). Ataxia-telangiectasia mutated kinase in the control of oxidative stress, mitochondria, and autophagy in cancer: a maestro with a large orchestra. *Front. Oncol.* **8**, 73.

Uziel, T., Savitsky, K., Platzer, M., Ziv, Y., Helbitz, T., Nehls, M., Boehm, T., Rosenthal, A., Shiloh, Y. and Rotman, G. (1996). Genomic organization of the ATM gene. *Genomics* **33**, 317-320.

Valentin-Vega, Y. A., Maclean, K. H., Tait-Mulder, J., Milasta, S., Dorsey, F. C., Cleveland, J. L., Green, D. R., Kastan, M. B., Dc, W. and Steeves, M. (2012). Mitochondrial dysfunction in ataxia-telangiectasia. *Blood* **119**, 1490-1500.

Voss, S., Pietzner, J., Hoche, F., Taylor, A. M. R., Last, J. I., Schubert, R. and Zielen, S. (2014). Growth retardation and growth hormone deficiency in patients with Ataxia telangiectasia. *Growth Factors* **32**, 1029-22923.

Xu, Y., Ashley, T., Brainerd, E. E., Bronson, R. T., Meyn, M. S. and Baltimore, D. (1996). Targeted disruption of A T M leads to growth retardation, chromosomal tragmentation during meiosis, immun e defects, and thymic lymphoma. *Genes Dev.*, **10**, 2411-2422.

Yang, D.-Q. and Kastan, M. B. (2000). Participation of ATM in insulin signalling through phosphorylation of eIF-4E-binding protein 1. *Nat. Cell Biol.* **2**, 893-898.